

<https://doi.org/10.1038/s42005-026-02489-8>

Smile-shaped electron gradient distributions observed during magnetic reconnection at Earth's magnetopause

Check for updates

Jason R. Shuster¹ ✉, Naoki Bessho^{2,3}, John C. Dorelli², Daniel J. Gershman², Jason M. H. Beedle¹, Harsha Gurram^{2,3}, Jonathan Ng^{2,3}, Li-Jen Chen², Roy B. Torbert¹, James L. Burch⁴, Barbara L. Giles², Richard E. Denton⁵, Paul A. Cassak⁶, M. Hasan Barbhuiya⁶, Steven J. Schwartz⁷, Yi-Hsin Liu⁵, Cecilia Norgren^{8,9}, Daniel E. da Silva^{2,10}, Kevin J. Genestreti⁴, Steven V. Heuer¹, Matthew R. Argall¹, Hanieh Karimi¹, Andy T. Marshall⁴, Rumi Nakamura¹¹, Haoming Liang^{2,3}, Vadim M. Uritsky¹², Arya Afshari¹³ & Dominic S. Payne¹⁴

The electron diffusion region is central to NASA's Magnetospheric Multiscale (MMS) mission to understand collisionless magnetic reconnection, the plasma physics phenomenon crucial to triggering the explosive energy release of solar flares, powering auroras generated in planetary magnetospheres, and driving sawtooth crashes in laboratory fusion devices. Inside the diffusion region, electron velocity distributions exhibit highly-structured velocity-space signatures critical for elucidating the kinetic mechanisms fueling reconnection. Recent multi-spacecraft analysis techniques enabled observational study of the spatial gradient in the electron velocity distribution, which has been reported in electron-scale current layers to explain the kinetic origins of electron pressure gradients. However, electron gradient distributions have not yet been investigated inside the reconnection diffusion region. In this work, we discover that electron gradient distributions exhibit a smile-shaped velocity-space structure in the electron diffusion region of asymmetric magnetic reconnection at Earth's magnetopause. Characterizing the nature and prevalence of these smile-shaped electron gradient distributions offers a kinetic perspective into how electrons spatially evolve to provide the net electron pressure divergence that self-consistently supports non-ideal electric fields in the electron diffusion region of magnetopause reconnection. These results are relevant to space, astrophysical, and laboratory plasma communities working to understand the long-standing mystery of collisionless magnetic reconnection.

The electron diffusion region (EDR) lies at the heart of NASA's four-spacecraft Magnetospheric Multiscale (MMS) mission to elucidate the kinetic mechanisms that fuel collisionless magnetic reconnection, the ubiquitous and explosive plasma phenomena operating throughout our universe to rapidly convert stored magnetic energy into plasma kinetic and thermal energy¹. On October 16, 2015, MMS observed the first EDR ever

detected in space with sufficient spatiotemporal resolution of the fields and plasma particles to definitively characterize electron kinetic structures during asymmetric reconnection occurring at Earth's dayside magnetopause², as illustrated schematically in Fig. 1a. Inside this EDR, MMS measured nongyrotropic crescent-shaped electron velocity distribution functions that were previously predicted by state-of-the-art kinetic particle-

¹Space Science Center, University of New Hampshire, Durham, NH, USA. ²Goddard Space Flight Center, NASA, Greenbelt, MD, USA. ³Department of Astronomy, University of Maryland, College Park, MD, USA. ⁴Southwest Research Institute, San Antonio, TX, USA. ⁵Department of Physics and Astronomy, Dartmouth College, Hanover, NH, USA. ⁶Department of Physics and Astronomy, Clemson University, Clemson, SC, USA. ⁷Department of Physics, Imperial College, London, UK. ⁸Swedish Institute of Space Physics, Uppsala, Sweden. ⁹Department of Physics and Technology, University of Bergen, Bergen, Norway. ¹⁰Goddard Planetary Heliophysics Institute, University of Maryland, Baltimore County, Baltimore, MD, USA. ¹¹Space Research Institute, Austrian Academy of Sciences, Graz, Austria. ¹²Department of Physics, Catholic University of America, Washington DC, USA. ¹³Department of Physics and Astronomy, University of Iowa, Iowa City, IA, USA. ¹⁴Department of Physics, University of Michigan, Ann Arbor, MI, USA. ✉e-mail: jason.shuster@unh.edu

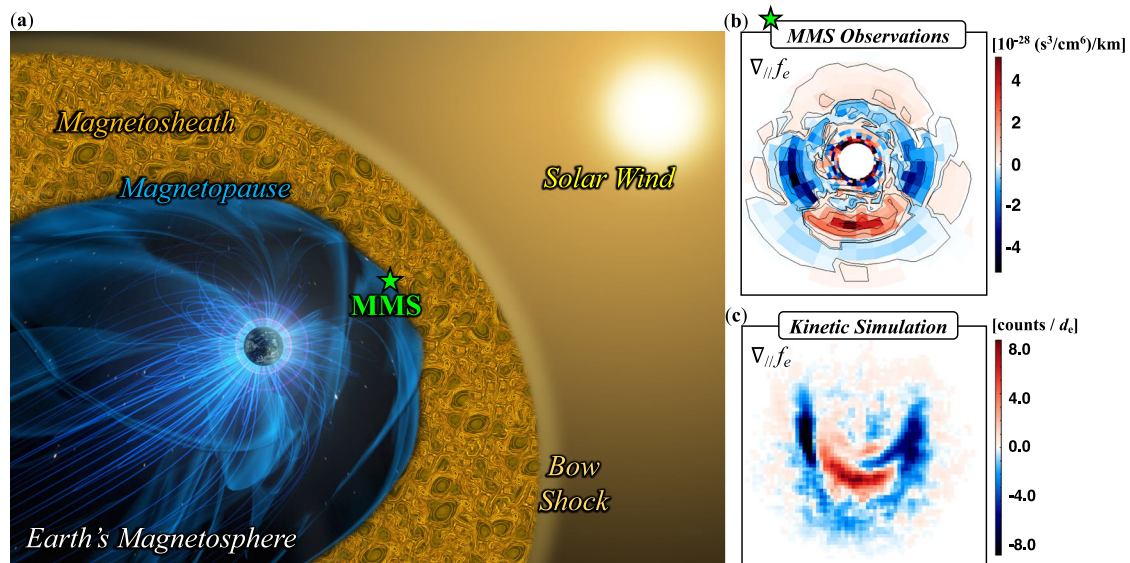


Fig. 1 | Smile-shaped electron gradient distributions observed in Earth’s magnetosphere. **a** Artist rendition of Earth’s magnetosphere (source: NASA Goddard Space Flight Center’s Scientific Visualization Studio³³) and the location of the Magnetospheric Multiscale (MMS) spacecraft when they observed **(b)** smile-shaped electron gradient distributions $\nabla_{||} f_e$ associated with crescent-shaped electron velocity distributions $f_e(\mathbf{v})$ in the electron diffusion region of magnetic reconnection at Earth’s dayside magnetopause on October 16, 2015. **c** Electron gradient distribution structures in $\nabla_{||} f_e$ predicted by kinetic particle-in-cell (PIC) simulations of

asymmetric magnetic reconnection, presented in detail in FigS. 2 and 3. The red (blue) color in the electron gradient distributions corresponds to an increase (decrease) in electron phase space density as a result of moving spatially through the plasma. The blue ‘eyes’ in the electron gradient distributions are regions in velocity-space where the electron phase space density decreases due to the crescent population’s reduction in gyrophase spread. The red ‘smile’ structure indicates that electrons in this region concentrate and narrow in velocity space, resulting in an intensification of electron phase space density.

in-cell (PIC) simulations and that have since become one of the hallmark signatures of fundamental electron kinetic processes associated with asymmetric reconnection and electron-scale current sheets^{2–7}. At the EDR in Earth’s nightside magnetotail, MMS also detects highly structured, agyrotropic electron distribution functions exhibiting triangular and discretely striated structures consistent with the characteristic demagnetized meandering motion predicted to arise in symmetric reconnection configurations^{8–12}. Observations of these types of distinct statistical structures in velocity space aid in pinpointing where spacecraft like MMS are located in relation to the underlying reconnection topology¹³, and they are indicative of the types of energy conversion mechanisms operating to accelerate and energize particles in those regions^{14–20}. These types of electron-scale plasma phenomena continue to surprise our research communities, especially in light of the recent results reporting “electron-only” reconnection and its properties discovered in the context of Earth’s turbulent magnetosheath environment (e.g.,^{21–25}).

Recent efforts have emphasized the wealth of information contained within phase space that has been largely unexplored due to the difficulty of interpreting these types of variations in phase space density measurements¹⁷. Despite the utility of characterizing coherent structures in electron distribution functions, the complexity of phase space sometimes allows for ambiguous interpretations. For instance, crescent-shaped electron distribution functions do not uniquely correspond to regions with electron meandering motion that one would typically associate with EDRs. In fact, electron crescent distributions are expected to be found in sufficiently thin electron-scale current layers due to the diamagnetic drift of well-magnetized electrons^{26,27}. This ambiguity raises several important questions: (1) How do we interpret the observations of electron crescent-shaped distributions given that they are a necessary but not sufficient indicator of electron meandering motion associated with the EDR of asymmetric reconnection? (2) When MMS observes electron crescent-shaped distributions determined to be associated with reconnection, how do we then infer their location with respect to the underlying reconnection geometries offered by theory and kinetic simulations?

The discoveries we report in this paper help to answer both of these questions. The key idea is to visualize and characterize velocity-space structures that appear when taking *derivatives* of the phase space density measurements. Rather than only considering the velocity-space structure of the electron distribution itself (i.e., $f_e(\mathbf{v})$), we consider how electron distribution structures change in time, space, and velocity-space (e.g., via the derivative quantities $\partial f_e / \partial t$, ∇f_e , and $\nabla_{||} f_e$). This approach requires utilizing the Fast Plasma Investigation (FPI) suite comprising 64 ion and electron particle spectrometers onboard the MMS spacecraft²⁸, and has been previously implemented to resolve spatiotemporal variations in the electron phase space density measurements taken from electron-scale current sheets embedded within Earth’s magnetopause^{7,29}. These techniques enable velocity-space visualization and observational comparison of each term in the Vlasov equation, which historically could only be studied via analytical and numerical approaches because the framework of kinetic theory is built in an abstract seven-dimensional phase space that could not previously be resolved observationally^{30–33}. Quantifying how the particle distribution function changes in each of those dimensions offers a promising way to distinguish the particle distribution signatures associated with reconnecting and non-reconnecting current sheets, allows for a more precise determination of the MMS location with respect to the EDR, and provides insight into the fundamentally kinetic energization mechanisms that fuel collisionless magnetic reconnection.

In this paper, we report the discovery of a surprising smile-shaped structure in the gradient of the electron distribution function (referred to as the electron gradient distribution) oriented parallel to the magnetic field measured by MMS during its first dayside EDR encounter (see Figs. 1b and 2g). This coherent smile-shaped structure is associated with previously reported electron-crescent distributions and large-amplitude parallel electric fields^{2,34}, and we find consistent and comparable structures in fully kinetic PIC simulations of asymmetric reconnection with a sufficiently large number of particles per cell⁴ needed to resolve such distinct and localized velocity-space variations (see Figs. 1c and 2i, j). In the PIC simulation, smile-shaped structures are found in electron gradient

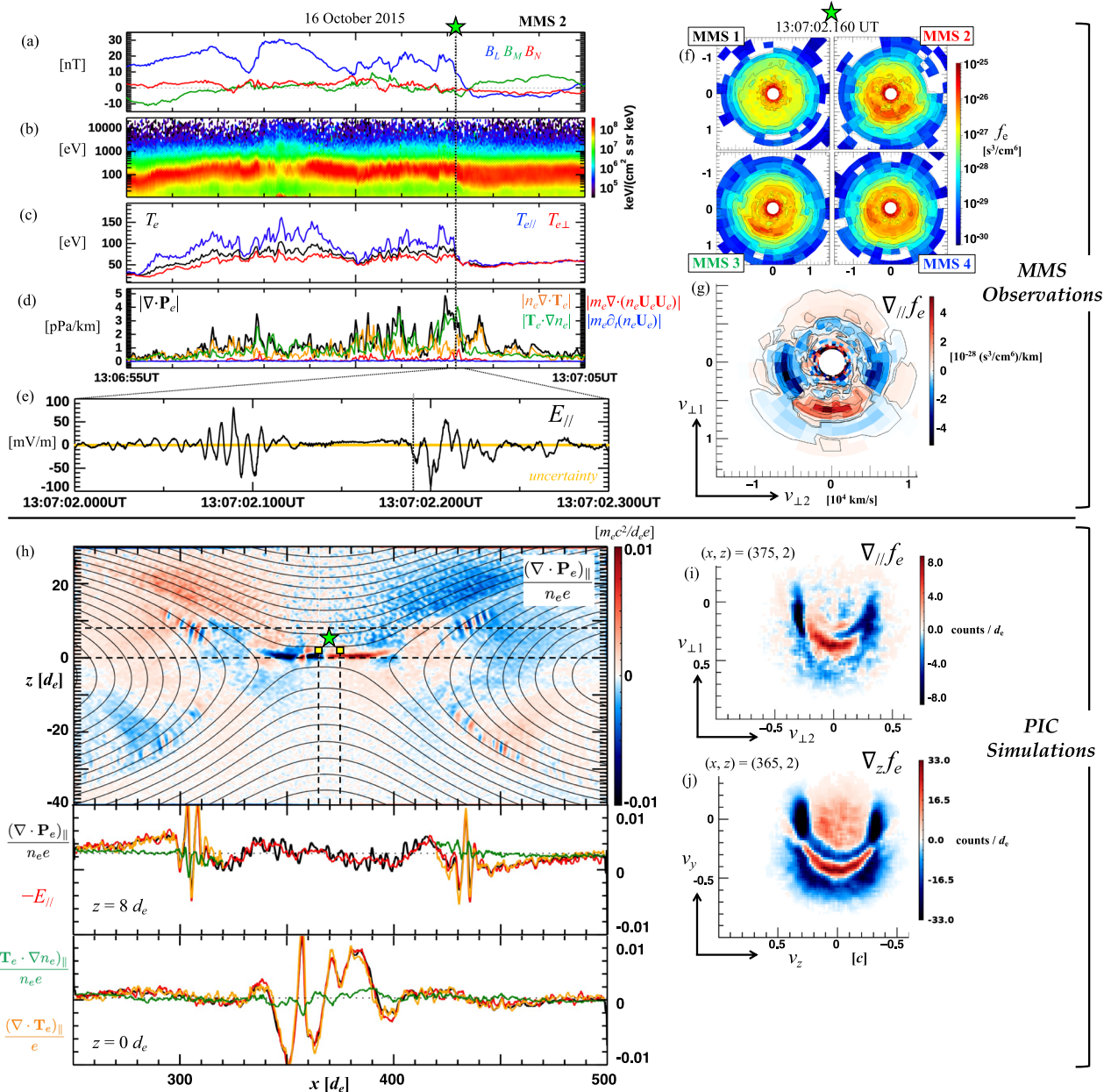


Fig. 2 | Multi-spacecraft observations and kinetic simulations of smile-shaped electron gradient distributions at Earth's magnetopause. a–c 10-second overview of Magnetospheric Multiscale (MMS) 2 measurements with a vertical dashed line and green star indicating the time of the electron distributions (f, g) on the right. **a** Magnetic field data from the fluxgate magnetometer (FGM) in boundary-normal (LMN) coordinates. The coordinate transformation is provided by ref. 2. **b** Electron omnidirectional energy spectrogram from the dual electron spectrometers (DES). **c** Electron temperatures: total T_e (black), perpendicular $T_{e\perp}$ (red), and parallel $T_{e\parallel}$ (blue). **d** Magnitudes of the electron pressure divergence $|\nabla \cdot \mathbf{P}_e|$ (black), its decomposition into the temperature divergence $|n_e \nabla \cdot \mathbf{T}_e|$ (orange) and density gradient $|\mathbf{T}_e \cdot \nabla n_e|$ (green) contributions computed from the four spacecraft, along with the inertial term's spatial divergence $|m_e \nabla \cdot (n_e \mathbf{U}_e \mathbf{U}_e)|$ (red) and the time derivative term $|m_e \partial_t (n_e \mathbf{U}_e)|$ (blue) computed from MMS 2 for reference. **e** Zoom-in view (0.3 seconds) of the high cadence parallel electric field E_{\parallel} from the electric field double probes (EDP) on MMS 2. **f** The four crescent-shaped electron velocity distributions f_e from the four MMS spacecraft used to compute (g) the smile-shaped electron gradient distribution oriented parallel to the magnetic field $\nabla_{\parallel} f_e$ at

13:07:02.160 UT indicated by the green star in (a–d). **h–j** Particle-in-cell (PIC) simulation results comparable to the MMS observations. **h** The 2D color plot shows the parallel electric field arising from the electron pressure divergence term $(\nabla \cdot \mathbf{P}_e)_{\parallel} / n_e e$. The 1D cut panels below taken along the dashed lines at $z = 8 d_e$ and $z = 0 d_e$ show $(\nabla \cdot \mathbf{P}_e)_{\parallel} / n_e e$ (black) balanced well by $-E_{\parallel}$ (red), and the dominant temperature divergence (orange) and density (green) gradient contributions. For the $z = 8 d_e$ cut, these gradient components are plotted for $x < 320 d_e$ and $x > 420 d_e$ to focus on the coherent separatrix structures in $(\nabla \cdot \mathbf{P}_e)_{\parallel} / n_e e$ rather than the noisier signal on the low-density ($z > 0$) side between $320 < x < 420$. **i** Smile-shaped electron gradient distribution in the parallel direction $\nabla_{\parallel} f_e$ taken at $(x, z) = (375, 2) d_e$ in the PIC domain indicated by the right yellow box in (h) to compare with the MMS gradient distribution above. **j** Prominent smile-shaped electron gradient distribution $\nabla_z f_e$ oriented perpendicular to the magnetic field taken at $(x, z) = (365, 2) d_e$ and indicated by the left yellow box in (h). Two electron crescent distributions are shown to the right from $z = 3 d_e$ and $z = 2 d_e$, illustrating how the crescent population varies spatially to produce the smile-shape.

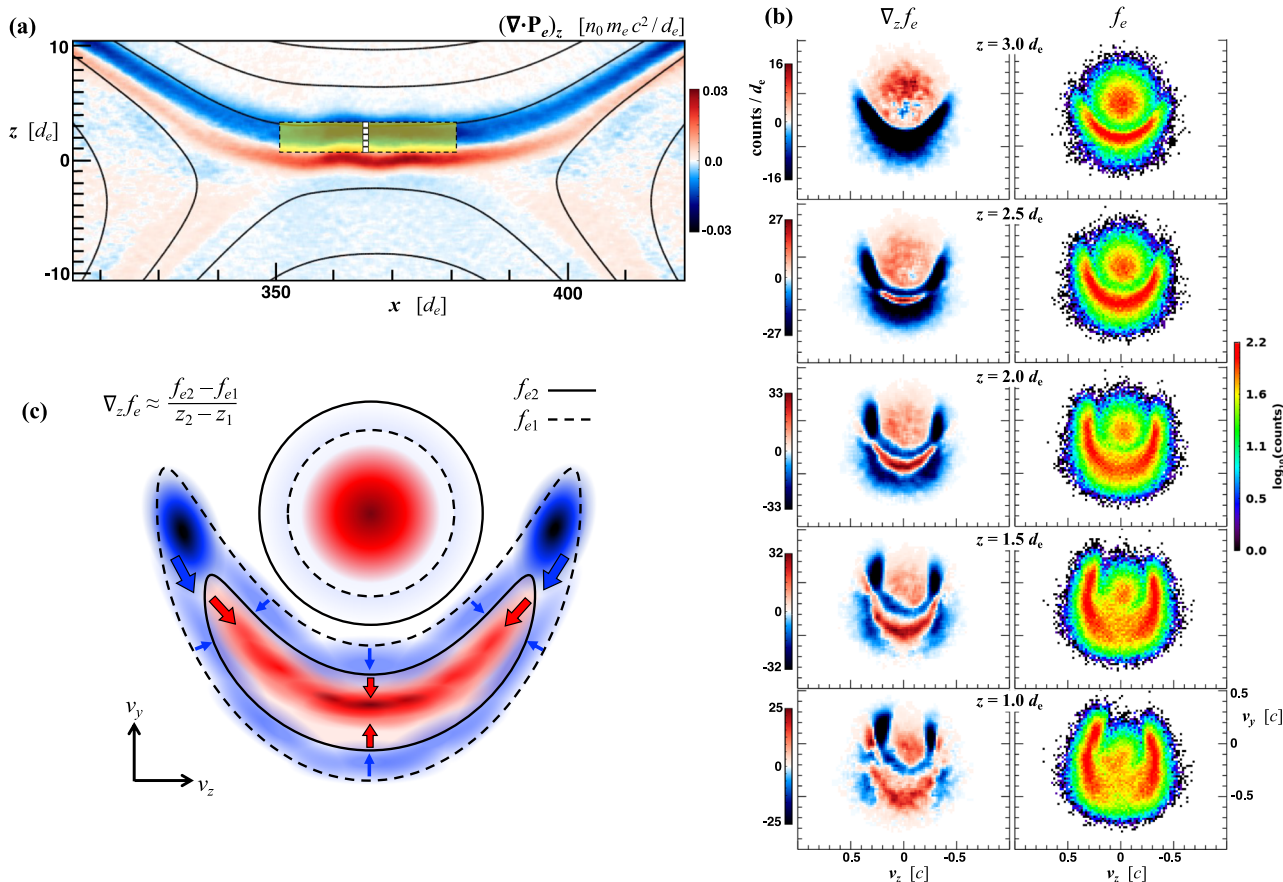


Fig. 3 | Velocity-space structure and formation of smile-shaped electron gradient distributions in the simulated electron diffusion region of asymmetric magnetic reconnection. **a** Zoom-in view of the particle-in-cell (PIC) simulation domain shown in Fig. 2h, here showing the z -component of the electron pressure divergence, $(\nabla \cdot \mathbf{P}_e)_z$, with a yellow region of size $\Delta x \times \Delta z = 30d_e \times 2d_e$ highlighting roughly where smile-shaped gradient distributions are found on the magnetospheric (low-density) side of the X-line. **b** Electron velocity distributions, f_e (right column), and their corresponding gradient distributions, $\nabla_z f_e$ (left column), taken at five varying z -locations as indicated by the small white boxes in (a). **c** Schematic representation of the smile-shaped velocity-space structure of $\nabla_z f_e$ near $z = 2d_e$. The blue (red) regions are where electron phase space density decreases (increases) while moving spatially in the $+z$ -direction. The blue (red) arrows further indicate how these coherent

regions of the gradient distribution move in velocity space as $\nabla_z f_e$ is sampled at increasing values of z , as shown by the spatial evolution evident in (b) and discussed in the Results section. The dashed outlines indicate representative model contours of f_{e1} taken near $z = 2d_e$, while the solid outlines denote contours of f_{e2} taken near $z = 3d_e$. The prominent blue ‘eyes’ form near the ends of the crescent-shaped population in f_e as the crescent’s angular gyrophase extent decreases. The red ‘smile’ forms at the center of the crescent population as electron phase space density concentrates there, leaving a blue, beard-like ‘halo’ region around the crescent. The more isotropic red ‘core’ of the gradient distribution forms as phase space density in the low-energy core population increases while moving away from the electron diffusion region (EDR) acceleration region.

distributions oriented both in the direction parallel and perpendicular to the magnetic field. The smile-shaped gradient distributions form in velocity-space as electron crescent-shaped distributions vary spatially: ‘eyes’ emerge as the crescent population’s gyrophase extent decreases, while the ‘smile’ appears due to an intensification of phase space density concentrated at the crescent’s center (see Fig. 3). Understanding the spatial and velocity-space characteristics regarding where and how smile-shaped electron gradient distributions develop is useful for precisely locating the MMS tetrahedron with respect to the magnetic reconnection topology of the electron-scale diffusion region, differentiating between reconnecting and non-reconnecting types of current layers, and advancing our understanding of how the electron pressure divergence balances non-ideal parallel electric fields in and around the electron diffusion region.

Results
Phase Space Density Gradients Supporting the Electron Diffusion Region of Asymmetric Magnetic Reconnection

We begin our discussion with the electron Vlasov equation, which describes the evolution of the electron distribution function, $f_e = f_e(\mathbf{x}, \mathbf{v}, t)$, throughout

phase space:

$$\frac{df_e}{dt} = \frac{\partial f_e}{\partial t} + \mathbf{v} \cdot \nabla f_e + \frac{\mathbf{F}}{m_e} \cdot \nabla_{\mathbf{v}} f_e = 0, \tag{1}$$

where $\mathbf{F} = -e(\mathbf{E} + \mathbf{v} \times \mathbf{B})$ is the Lorentz force on an electron, e is the fundamental charge, and m_e is the electron mass (e.g., see ref. 35). Taking the first moment of the Vlasov equation by first multiplying Equation (1) by the velocity-space coordinate \mathbf{v} and then integrating over velocity space, one readily obtains the electron momentum equation (i.e., generalized Ohm’s law) describing the macroscopic force balance on the bulk electron fluid:

$$n_e e(\mathbf{E} + \mathbf{U}_e \times \mathbf{B}) = -\nabla \cdot \mathbf{P}_e - \nabla \cdot (m_e n_e \mathbf{U}_e \mathbf{U}_e) - \frac{\partial}{\partial t} (m_e n_e \mathbf{U}_e), \tag{2}$$

where n_e is the electron density, \mathbf{U}_e is the electron bulk velocity, and \mathbf{P}_e is the electron pressure tensor.

To develop intuition concerning the expected importance of each term at Earth’s dayside magnetopause, consider the following order of magnitude estimates for the three terms on the right hand side of Equation (2). A strong

electron bulk velocity jet is on the order of 1000 km/s and is frequently observed by MMS over a duration of roughly 0.1 s, along with a steady density of 10 cm^{-3} . Thus, the magnitude of the time derivative term $\frac{\partial}{\partial t}(m_e n_e \mathbf{U}_e)$ is on the order of $m_e (10 \text{ cm}^{-3}) (1000 \text{ km/s}) / (0.1 \text{ s}) \approx 0.1 \text{ pPa/km}$. For the spatial gradient portion of the inertial term $\nabla \cdot (m_e n_e \mathbf{U}_e \mathbf{U}_e)$, a similar order of magnitude estimate for a 1000 km/s electron jet arising on electron-scales of roughly 10 km (i.e., a few electron skin depths, which is commonly the interspacecraft separation of MMS), we find $m_e (10 \text{ cm}^{-3}) (1,000 \text{ km/s}) (1,000 \text{ km/s}) / (10 \text{ km}) \approx 1.0 \text{ pPa/km}$. For the electron pressure divergence term $\nabla \cdot \mathbf{P}_e$, assuming a steady density and increasing temperature of roughly 60 eV (i.e., the electron temperature is observed to roughly double from 60 eV to 120 eV for the event studied here) over this same 10 km spatial scale, we find: $(10 \text{ cm}^{-3}) (60 \text{ eV}) / (10 \text{ km}) \approx 10 \text{ pPa/km}$. For the event studied in this paper, we find results consistent with these order of magnitude estimates for each term, as shown in Fig. 2d: the maximum $\nabla \cdot \mathbf{P}_e$ is close to 5 pPa/km, while the maximum $\nabla \cdot (m_e n_e \mathbf{U}_e \mathbf{U}_e)$ is close to 1 pPa/km, and the maximum $\frac{\partial}{\partial t}(m_e n_e \mathbf{U}_e)$ is close to 0.1 pPa/km. Therefore, we expect that the relative importance of these terms for electron-scale current layers like the event studied in this paper differs by successive orders of magnitude, with the $\nabla \cdot \mathbf{P}_e$ term being dominant throughout the majority of the interval. Thus, to a reasonable approximation in this context, it is most important to study the role of the electron pressure divergence term in the electron momentum equation:

$$n_e e(\mathbf{E} + \mathbf{U}_e \times \mathbf{B}) \approx -\nabla \cdot \mathbf{P}_e. \quad (3)$$

Furthermore, when considering the component of this equation that is parallel to the magnetic field, \mathbf{B} , we see that the non-ideal parallel electric field, E_{\parallel} , is balanced by the parallel component of the electron pressure divergence ($\nabla \cdot \mathbf{P}_e$)_∥ in the following way:

$$E_{\parallel} \approx -\frac{(\nabla \cdot \mathbf{P}_e)_{\parallel}}{n_e e} = -\frac{1}{e} \left[\frac{(\mathbf{T}_e \cdot \nabla n_e)_{\parallel}}{n_e} + (\nabla \cdot \mathbf{T}_e)_{\parallel} \right], \quad (4)$$

where $\mathbf{T}_e = \mathbf{P}_e/n_e$ is the electron temperature tensor (in units of energy so that we neglect writing Boltzmann's constant k_B), and we have decomposed the electron pressure term into its contributions from the density gradient $\frac{(\mathbf{T}_e \cdot \nabla n_e)_{\parallel}}{n_e e}$ and temperature divergence $\frac{(\nabla \cdot \mathbf{T}_e)_{\parallel}}{e}$ terms. It is critical to determine the kinetic origins of large (100s of mV/m) non-ideal parallel electric fields observed by MMS associated with the EDR and other electron-spatial-scale events³⁴. While previous studies have focused on the perpendicular spatial gradient term $\nabla_{\perp} f_e$ as it relates to perpendicular components of the electron pressure divergence^{7,30}, here we consider the velocity-space structure of the electron gradient distribution parallel to the magnetic field, $\nabla_{\parallel} f_e$. Taking the first moment of the Vlasov equation (e.g., see refs. 7,35), we see how both $\nabla_{\parallel} f_e$ and $\nabla_{\perp} f_e$ contribute to the parallel component of the electron pressure divergence ($\nabla \cdot \mathbf{P}_e$)_∥ that self-consistently balances E_{\parallel} :

$$-en_e E_{\parallel} \approx (\nabla \cdot \mathbf{P}_e)_{\parallel} \approx m_e \int v_{\parallel} (\mathbf{v} \cdot \nabla f_e) d^3 v \approx m_e \int (v_{\parallel}^2 \nabla_{\parallel} f_e + v_{\parallel} v_{\perp 2} \nabla_{\perp 2} f_e) d^3 v, \quad (5)$$

where here we assume that variation along one of the perpendicular spatial coordinate directions $x_{\perp 1}$ is small compared to that of the other, $x_{\perp 2}$ (see the Methods section for more details regarding the definition of these magnetic field-aligned coordinates). This assumption is valid, for instance, when $x_{\perp 1}$ is close to the non-varying out-of-plane direction in a typical 2.5D PIC simulation and commonly occurs for electron-scale structures near the magnetopause (e.g.,^{7,30}) so that $v_{\parallel} v_{\perp 2} \nabla_{\perp 2} f_e$ dominates and we may neglect the contribution from the $v_{\parallel} v_{\perp 1} \nabla_{\perp 1} f_e$ term. Additionally, supported by the order of magnitude estimates above, we assume that for most of the electron velocity-space of interest, $v \gg U_e$, so that we may neglect the $\nabla \cdot (m_e n_e \mathbf{U}_e \mathbf{U}_e)$ term, which is reasonable for typical magnetopause and magnetosheath events where it is often the case that $v_{e,th} > U_e$ (i.e., the electron thermal speed $v_{e,th} \approx 5000 \text{ km/s}$ to $10,000 \text{ km/s}$ is commonly one to two orders of

magnitude larger than the electron bulk velocity $U_e \approx 100 \text{ km/s}$ to 1000 km/s). Thus, Equation (5) gives an approximate integral relationship between the critical macroscopic quantities E_{\parallel} and $(\nabla \cdot \mathbf{P}_e)_{\parallel}$, and their kinetic counterparts: the dominant contributing gradient distributions $\nabla_{\parallel} f_e$ and $\nabla_{\perp 2} f_e$. In the next section, utilizing MMS observations and PIC simulations, we investigate the kinetic properties of these gradient distributions, $\nabla_{\parallel} f_e$ and $\nabla_{\perp 2} f_e$, and how they self-consistently sustain E_{\parallel} and $\nabla \cdot \mathbf{P}_e$ in the EDR of asymmetric magnetic reconnection at Earth's magnetopause.

Smile-Shaped Electron Gradient Distributions Discovered in the EDR with MMS Observations and PIC Simulations

We present an investigation of these electron gradient distribution terms in Fig. 2 from the perspective of both MMS observations and PIC simulations of the EDR. We commence our analysis of EDR electron gradient distribution signatures by focusing on the most well-established EDR event studied thus far: the October 16, 2015 event². At 13:07:02 UT, MMS encountered this EDR during asymmetric reconnection at Earth's dayside magnetopause, which we illustrate schematically in Fig. 1a and show in Fig. 2a–d for MMS 2 measurements. Close to the reconnecting magnetic field component's reversal (B_L in Fig. 2a), the Electric Field Double Probes (EDP) on MMS 2 detected large-amplitude (on the order of ~ 100 of mV/m) fluctuations in the non-ideal parallel electric field, E_{\parallel} , shown in the zoom-in view of Fig. 2e. At this time, MMS 2 sees a significant electron temperature divergence, especially in the parallel electron temperature (Fig. 2c), and a substantial electron pressure divergence $|\nabla \cdot \mathbf{P}_e| \sim 5 \text{ pPa/km}$ (Fig. 2d). This divergence in the electron pressure appears at 13:07:02 UT due primarily to an electron density gradient (green trace) arising from the $(\mathbf{T}_e \cdot \nabla n_e)_{\perp 2}$ component, and then due to the electron temperature divergence (orange trace) mainly from $(n_e \nabla \cdot \mathbf{T}_e)_{\perp 2}$ less than a second afterward (just before 13:07:03 UT). At 13:07:02 UT, there is a parallel electron pressure divergence $(\nabla \cdot \mathbf{P}_e)_{\parallel}$ of about 1 pPa/km due to the parallel component of the temperature divergence term $n_e (\nabla \cdot \mathbf{T}_e)_{\parallel}$.

At the time indicated by the green star (Fig. 2a–d) and the vertical dashed line in Fig. 2e, the Fast Plasma Investigation (FPI) observed the four electron velocity-space distribution functions, f_e , shown in Fig. 2f, and the smile-shaped electron gradient distribution parallel to the magnetic field $\nabla_{\parallel} f_e$ shown in Fig. 2g computed by utilizing the four-spacecraft MMS tetrahedron to obtain the spatial derivative of these electron phase space density measurements^{7,30}. At this time, MMS 2 and MMS 3 observe crescent-shaped distributions, MMS 4 sees a ring-like distribution, and MMS 1 sees a more isotropic distribution compared to the other three spacecraft (Fig. 2f). Computing the spatial gradient distribution ∇f_e from these four electron distributions and projecting that vector along the magnetic field direction yields the parallel gradient distribution $\nabla_{\parallel} f_e = (\nabla f_e) \cdot \hat{\mathbf{b}}$ shown in Fig. 2g. The blue 'eyes' located near $(v_{\perp 1}, v_{\perp 2}) = (0, \pm 5000) \text{ km/s}$ indicate that electron phase space density decreases (roughly at a rate of $-4 \times 10^{-28} \text{ (s}^3/\text{cm}^6)/\text{km}$) in these regions of velocity space in the direction parallel to the magnetic field. In the red 'smile' region of velocity space near $(v_{\perp 1}, v_{\perp 2}) = (5000, 0) \text{ km/s}$, electron phase space density increases (roughly at a rate of $+4 \times 10^{-28} \text{ (s}^3/\text{cm}^6)/\text{km}$) in the direction of the magnetic field. MMS observes this type of smile-shaped structure in $\nabla_{\parallel} f_e$ for five consecutive DES time steps for about 0.15 seconds. Knowing the magnetic structure velocity was approximately 100 km/s for this event³⁶, we obtain a lower bound for estimating the length of the smile-shaped region, L , as follows: $L \approx (100 \text{ km/s})(0.15 \text{ s}) = 15 \text{ km}$, which is on the order of $10 d_e$. We also note that MMS does not observe a smile-shaped structure in the perpendicular gradient component, $\nabla_{\perp 2} f_e$, for this event. Instead, MMS observes $\nabla_{\perp 2} f_e$ structures similar to those reported in prior studies of electron-scale current layers^{7,30,31}.

To better understand how to interpret this smile-shaped gradient distribution structure in $\nabla_{\parallel} f_e$ as it relates to the crescent-shaped distributions associated with EDR dynamics, next we analyze the 2.5D PIC simulation results for asymmetric reconnection shown in the panels below (Fig. 2h–j). The simulation is performed with 3000 particles per cell, a computationally expensive parameter choice to increase the signal-to-noise

ratio for the velocity-space structures of interest, like crescent-shaped distributions known to develop more prominently on the low-density (magnetospheric) side of the asymmetric reconnection EDR⁴. Spatial locations are reported in units of the electron skin depth, d_e . Figure 2h shows the spatial profile of the parallel component of the electron pressure divergence term $(\nabla \cdot \mathbf{P}_e)_\parallel / n_e e$ that predominantly balances E_\parallel throughout the reconnection region. The first panel below Fig. 2h shows several cuts taken along $z = 8d_e$ of $-E_\parallel$ (red trace) and $(\nabla \cdot \mathbf{P}_e)_\parallel / n_e e$ (black trace) in order to highlight the fluctuations on the magnetospheric separatrix that develop near $(x, z) = (300, 8) d_e$ and $(x, z) = (430, 8) d_e$. When decomposing the pressure divergence into its density gradient (green trace) and temperature divergence (orange trace) contributions as we did for the MMS data in Fig. 2d, we see that these E_\parallel fluctuations are largely supported by the parallel component of the electron temperature divergence $(\nabla \cdot \mathbf{T}_e)_\parallel / e$. The second panel features cuts of the same quantities at $z = 0d_e$, showing that the electron temperature divergence term is also the dominant term supporting the enhanced $(\nabla \cdot \mathbf{P}_e)_\parallel / n_e e$ and hence E_\parallel structures extending throughout the EDR and electron outflow near $z = 0$ from $x = 330d_e$ to $x = 400d_e$. Note that near $(x, z) = (355, 0) d_e$, there is a small secondary electron-scale magnetic island forming that causes localized fluctuations in $(\nabla \cdot \mathbf{P}_e)_\parallel$ there.

The smile-shaped gradient distributions (Fig. 2i and j) taken at $(x, z) = (365, 2) d_e$ and $(x, z) = (375, 2) d_e$ in the EDR (marked with yellow boxes in Fig. 2h) appear close to the large amplitude E_\parallel signatures that peak close to the X-point and extend downstream along the electron exhaust (roughly from $x = 340 d_e$ to $400 d_e$ near $z = 0 d_e$). For reference, the green star is plotted between the locations of these two gradient distributions in Fig. 2h on the magnetospheric (low-density, $z > 0$) side of the X-line at a location consistent with previous modeling of the MMS trajectory^{2,13}. The average separation between the MMS spacecraft for this event was approximately 10 km², which is roughly 5 d_e (using the density observed by MMS 2: $n_e \approx 7 \text{ cm}^{-3}$). When we select a gradient scale length of 5 d_e in the PIC simulation, we find discernible smile-shaped structures emerging in the $\nabla_\parallel f_e$ distributions that are comparable to the MMS observations (compare Fig. 2g to i). At the location of the PIC $\nabla_\parallel f_e$ distribution $(x, z) = (375, 2) d_e$ marked by the rightmost yellow box in Fig. 2h, the magnetic field (see black contours in Fig. 2h) points mainly along the x -direction. Thus, the method for computing $\nabla_\parallel f_e$ in the PIC simulation at this location is approximately the same as estimating $\partial f_e / \partial x$ via the finite difference estimation of the distributions taken at $(x_2, z_2) = (380, 2) d_e$ and $(x_1, z_1) = (375, 2) d_e$ as follows: $\partial f_e / \partial x \approx (f_{e2} - f_{e1}) / \Delta x$, where we set $\Delta x = 5d_e$ to match the MMS spacecraft separation.

An even more prominent smile-shaped distribution structure develops in the PIC simulation in the direction normal to the current layer along the initial density asymmetry direction (i.e., along the z -direction), even though MMS did not detect a smile-shaped structure in this component (i.e., in $\nabla_{\perp 2} f_e$). This smile-shaped gradient distribution in the simulation ($\nabla_z f_e = \partial f_e / \partial z \approx (f_{e2} - f_{e1}) / \Delta z$, where $\Delta z = z_2 - z_1$) is shown in Fig. 2j, and its location at $(x, z) = (365, 2) d_e$ is indicated by the leftmost yellow box in Fig. 2h. To see how this gradient distribution structure forms, Fig. 3b shows a series of five f_e -distributions (right column) alongside their corresponding gradient distributions $\nabla_z f_e$ (left column) taken from $z = 1d_e$ to $z = 3d_e$. From these crescent distributions, we can see how the dark blue ‘eye’-regions and the red ‘smile’-region in Fig. 3b (repeated from Fig. 2j) form in velocity space. As the distribution function evolves spatially along the $+z$ -direction, we notice that (1) the gyrophase extent of the electron crescent population decreases (i.e., the angular extent of the crescent region shrinks from roughly 180° at $z = 2d_e$ to 120° at $z = 3d_e$), and (2) the phase space density toward the center of the crescent becomes more concentrated (i.e., the thickness of the crescent shape becomes narrower in velocity space). These spatial changes in f_e also explain the formation of the smile-shaped structure in $\nabla_\parallel f_e$ in Fig. 2i, except that because spatial variations are largest in the z -direction, the spatial separation needed to resolve $\nabla_z f_e$ is smaller ($\Delta z = 1d_e$). Due to the overall thinning of the crescent region and intensification of electron phase space density at the crescent’s center, there is also a resulting blue, beard-like ‘halo’ region with $\nabla_z f_e < 0$ that surrounds the red smile region. Additionally,

the simulated distribution in Fig. 2j exhibits a fainter red region with $\nabla_z f_e > 0$ that corresponds to the lower energy (centered at $v = 0$) mostly isotropic core of the distribution increasing in phase space density. This property of the gradient distribution’s core is likely due to a combination of two effects: (1) the density asymmetry across the EDR, and (2) the acceleration of lower-energy electrons (in the $-v_y$ direction) due to the reconnection electric field. The lower energy core of the MMS distribution in Fig. 2g cannot be reliably compared to the simulated distribution in this region of velocity-space because of photoelectron contamination of the Dual Electron Spectrometers (DES)³⁷.

Smile-shaped gradient distributions are found in the PIC simulation within a narrow band roughly of width 2 d_e in z from $z = 1 d_e$ to $z = 3 d_e$ and length 30 d_e in x extending from $x = 350 d_e$ to $x = 380 d_e$, as indicated by the yellow highlighted region in the spatial plot in Fig. 3a, which is consistent with the lower bound length estimate provided by the MMS observations. Below the smile-region ($z < 1d_e$), the distinct velocity-space features of the smile-shape are not yet recognizable. The smile-shape first becomes discernible in $\nabla_z f_e$ at $z \approx 1d_e$. By $z = 2d_e$, the gradient distribution’s blue ‘eyes’ and red ‘smile’ are fully formed in velocity space, as shown by the evolution in Fig. 3b. The blue and red arrows in Fig. 3c indicate how the coherent ‘eye’ and ‘smile’ regions move in velocity-space as the gradient distribution’s sampling location is moved upward to higher z -locations. As the f_e -crescent population reduces in gyrophase, the blue ‘eyes’ follow and demarcate the shrinking crescent region’s edges. Meanwhile, the red region of increasing and concentrating phase space density at the crescent’s center continues to occupy less of the velocity space, until the red ‘smile’ region vanishes completely as it becomes engulfed by the dark blue ‘eyes’ merging with the growing beard-like ‘halo’ region. Beyond this point, roughly in the range $3d_e < z < 5d_e$, the entire crescent-shaped region of velocity-space is blue ($\nabla_z f_e < 0$), indicating that the crescent-shaped electron population in f_e is diminishing in phase space density, which is expected when exiting the current layer. The uniform sign of the velocity-space crescent in $\nabla_z f_e$ in this spatial region closely resembles previous MMS observations of $\nabla_{\perp 2} f_e$ in electron-scale current layers (for examples, see distribution B5 of Figure 3 in ref. 7, and Figure 5g in ref. 30).

Discussion

The discovery of smile-shaped velocity-space structures in the electron gradient distribution terms responsible for sustaining the electron pressure divergence and parallel electric fields in the EDR offers kinetic insights for our space and laboratory plasma physics communities concerned with the longstanding question of how magnetic reconnection can operate in collisionless plasma environments. While visualizing particle distribution functions in velocity space is valuable, considering only the distribution function at one spatial location offers no information about spatial variations of the distribution that support critical processes, such as gradients in the electron pressure tensor components that sustain the reconnection electric field, analogously to how knowing the value of a function, $f(x)$, at one point x does not by itself provide information about its derivative, $f'(x)$. Using the EDR event considered here as an example, one could not predict the surprising smile-shaped pattern that emerges in ∇f_e from consideration of the crescent-shaped structure of $f_e(\mathbf{v})$ alone, as evidenced by the spatial evolution shown in Fig. 3b.

The results in this paper, along with other recent efforts (e.g., see refs. 17,18,31), chart future research directions toward successfully measuring, simulating, and understanding the behavior of all three terms in the Vlasov equation for collisionless plasmas in the context of the reconnection diffusion region, critical for breaking Alfvén’s frozen-in condition. PIC predictions enable us to fly virtual MMS-like detectors throughout the simulated reconnection domain to quantify the sensitivity of spatial and velocity-space binsize instrument design choices, which we may subsequently optimize via consideration of kinetic velocity-space entropy and associated information loss effects³⁸. The extensive MMS dataset sampled from the natural collisionless plasma laboratory of Earth’s magnetosphere is ripe for studying how kinetic structures develop and evolve in fully 3D environments, something

which recent 3D PIC simulations and global modeling efforts seek to emulate^{39–41}. For instance, the ability to model electron phase space density gradient distributions in a sufficiently large 3D PIC domain may allow us to better understand when and where smile-shaped structures occur in both parallel and perpendicular electron gradient distributions.

The first reports of electron gradient distribution (∇f_e) signatures were explained via simplified Maxwellian models that accounted for the various bipolar and quadrupolar velocity-space structures associated with crescent-shaped f_e -distributions observed by MMS in non-reconnecting, electron-scale current sheets^{7,30,31}. The highly-structured, smile-shaped, electron gradient distribution structures reported in this paper were not observed in those prior event studies, suggesting that the smile-shaped signatures may be unique to the electron diffusion region (EDR) of asymmetric reconnection. This hypothesis can be readily tested via future MMS and simulation studies that investigate the electron gradient distribution signatures observed in multiple EDR events for various upstream conditions. Any region where the electron crescent-shaped distribution evolves spatially in the manner illustrated in Fig. 3 ought to produce a smile-shaped electron gradient distribution signature in velocity space. However, the combination of both the crescent population's change in the gyrophase extent (leading to the blue 'eyes') and the intensification of electron phase space density concentrated at the crescent's center (leading to the inner red 'smile') may be difficult to find outside of the EDR in regions where magnetized electrons may not be able to exhibit such intricate velocity-space structures. Furthermore, the distinct and intricate velocity-space signatures of these smile-shaped gradient distributions, when observed, help to precisely orient the MMS spacecraft within the EDR of asymmetric reconnection in the same way that the detection of triangular, striated electron distributions provides strong evidence that MMS encountered the central EDR of symmetric reconnection^{8–12}.

The smile-shaped electron gradient distributions in $\nabla_{\parallel} f_e$ and $\nabla_{\perp} f_e$ arise as a result of spatially evolving electron crescent-shaped distributions, which themselves are kinetic manifestations in velocity-space that are directly associated with electron acceleration processes in the diffusion region of asymmetric reconnection geometries (e.g., see refs. 3,5). The mathematical connection presented in Equation (5) illustrates how both $\nabla_{\parallel} f_e$ and $\nabla_{\perp} f_e$ directly contribute to the net parallel component of the electron pressure divergence, $(\nabla \cdot \mathbf{P}_e)_{\parallel}$, and hence the non-ideal parallel electric field, E_{\parallel} . The intricate smile-shaped structures captured by the MMS observations and modeled in the PIC simulation provide a perspective to visualize how electrons are distributed in velocity space and how they evolve spatially in the dayside reconnection EDR to produce the net electron pressure gradient needed to balance E_{\parallel} .

A natural extension of the case-study presented in this work is to examine the electron gradient distribution signatures for the other reported dayside EDR events (e.g., see ref. 42) in order to identify potential statistical dependencies on various plasma parameters of interest, such as the guide field strength and density asymmetry ratio of asymmetric reconnection. As the guide field increases, electrons are expected to become increasingly magnetized and hence exhibit more gyrotropic velocity-space structures⁴³, thus nongyrotropic electron crescent signatures are expected to be less apparent in the large-guide field regime. Nevertheless, the sensitivity of the gradient distribution computation may resolve even relatively small phase space density differences between spatially separated distributions (e.g., such as the subtle phase space signatures associated with reconnection onset⁴⁴). Additionally, in light of recent progress understanding the phase space contribution to the pressure tensor in the well-known symmetric reconnection EDR found during magnetotail reconnection^{11,45}, an important next step would be to characterize the phase space density gradient distributions for that event and other MMS observations of the EDR in symmetric reconnection, although the lower plasma densities (and hence lower particle count rates for the FPI spectrometers) in Earth's magnetotail region may make it difficult to adequately resolve the gradient structures in velocity-space. While large-amplitude parallel electric fields have been associated with complicated, tangled magnetic fields requiring a fully 3D geometry to develop (e.g., see ref. 34), here we find qualitative agreement between the

MMS observations and 2.5D PIC simulations of the electron gradient distributions throughout most of velocity-space. This agreement may be because the guide field in the MMS event is small and assumed to be zero in the PIC simulation, which likely allows for more phase space symmetries to develop and persist (e.g., see ref. 46).

It remains unclear why MMS did not observe smile-shaped structures in the perpendicular gradient component, $\nabla_{\perp} f_e$, while that component (∇f_e) featured an even more prominent smile-shaped structure in the PIC simulation. Nevertheless, we speculate that MMS observed the smile-shapes in $\nabla_{\parallel} f_e$ because the reconnection structure was moving predominantly in the L -direction (i.e., in our simulation's x -direction, parallel to the reconnecting magnetic field component) at this time³⁶. Thus, MMS would have sampled more spatial locations parallel to the magnetic field rather than perpendicular to it. The MMS trajectory in the EDR for this event was mostly along our simulation's x -direction (see Fig. 3k of²), unlike the vertical path along $+z$ for the spatial evolution shown in Fig. 3b. Furthermore, given that the width of the region of smile-shaped gradient distributions predicted in the PIC simulation is only about $2d_e$ (roughly 2 or 3 km) in z along the normal direction, which is narrow compared to the average MMS spacecraft separation of 10 km (roughly 7 to 10 d_e), it would therefore be difficult for multiple MMS spacecraft to simultaneously occupy this region as would be necessary in order to resolve the gradient structure along the normal direction. An alternate possibility is that there may be inherently three-dimensional structure to the gradient distributions observed by MMS for this event that cannot be fully captured by a 2D PIC simulation, a situation which motivates future studies of electron distributions and their gradients in fully 3D PIC simulations for comparison with the MMS observations. Despite this discrepancy, the notable qualitative consistency of the smile-shaped structure throughout the velocity-space accessible to the MMS spacecraft and simulated in the PIC simulation, which together constitute the state-of-the-art capability in spacecraft detection and theoretical modeling, is especially encouraging and relevant to heliospheric, space, and laboratory plasma communities.

This work is directly relevant to the successfully launched TRACERS satellites and their science objectives to distinguish between the temporal and spatial variations of dayside magnetic reconnection inferred via multi-point measurements of accelerated plasma flows propagating along magnetic fields in Earth's highly dynamic cusp regions⁴⁷. In coordination with MMS multi-spacecraft measurements of the detailed kinetic signatures that manifest in the spatial gradient of the distribution function like those reported here, future conjunction studies utilizing both MMS and TRACERS present our field with a valuable opportunity to study and quantify how magnetic reconnection drives our near-Earth space weather environment by connecting measurements taken from the heart of the reconnection diffusion region to Earth's polar cusps where accelerated, reconnection-driven plasma outflows generate beautiful and mysterious auroral phenomena.

Methods

MMS Instrumentation

The spatial, temporal, and velocity-space resolution of the instrumentation onboard the MMS tetrahedron that enabled the discoveries reported in this paper include the Fast Plasma Investigation (FPI) for measuring 3D velocity-space electron and ion distribution functions at 30 ms and 150 ms, respectively²⁸, the Electric Field Double Probes (EDP) that measure high-resolution parallel electric fields at 8,192 Hz⁴⁸, and the Flux Gate Magnetometers (FGM) that provide magnetic field measurements at a cadence of 128 Hz^{49,50}.

PIC Simulation

The 2.5D particle-in-cell (PIC) simulation that resolved the smile-shaped velocity-space structures of the electron gradient distributions was initialized with the same parameters implemented in a previous study of electron crescent-shaped distributions associated with the EDR of asymmetric magnetic reconnection⁴. The average initial number of particles per cell was set to 3,000, sufficiently large for resolving the intricate velocity-space

structures of the electron distributions and their gradients within the EDR as reported in this paper. The density ratio across the current layer is set to $n_{MSH}/n_{MSP} = 8$, the magnetic field ratio to ensure pressure balance is $B_{MSP}/B_{MSH} = 1.37$, and the guide field is set to zero $B_g = 0$, where “MSH” denotes the high density magnetosheath side of the layer ($z < 0$), and “MSP” denotes the low density magnetospheric side ($z > 0$). The initial electron plasma to cyclotron frequency on the MSH side is: $\omega_{pe}/\Omega_{ce} = 2$, the ion to electron temperature ratio is $T_i/T_e = 2$, and the ion to electron mass ratio is $m_i/m_e = 100$. The boundary conditions in the outflow x -direction are periodic, while in the z -direction they are conducting for fields and reflecting for particles. The domain size is $75d_i \times 25d_i$ with 3072×2048 cells. All PIC data presented are taken from time $t\Omega_{ci} = 68$ less than $10 \Omega_{ci}^{-1}$ after peak reconnection. The binsize used to accumulate the distributions is $0.5d_e \times 0.5d_e$.

Coordinate Systems

The MMS magnetic field vector shown in Fig. 2a is plotted with the same boundary-normal (“LMN”) coordinates used in the first report of this EDR event². The electron distributions shown in Fig. 2f and g are plotted in local field-aligned coordinates, where v_{\parallel} is along the magnetic field direction \mathbf{B} , $v_{\perp 1}$ points along the direction of $(-\mathbf{U}_e \times \mathbf{B}) \times \mathbf{B}$, and $v_{\perp 2}$ completes the right-handed system by pointing along $-\mathbf{U}_e \times \mathbf{B}$. The PIC simulation is setup in boundary-normal coordinates with $+x$ along the outflow and reconnecting magnetic field direction (i.e., the L -direction), $+z$ along the direction normal to the current layer (i.e., the N -direction), and $+y$ completing the right-handed system by pointing into the page along the initial current layer (i.e., the M -direction).

Computing and interpreting the electron gradient distribution ∇f_e

The methodology for computing the electron gradient distribution ∇f_e vector with FPI has been reported previously (see⁷ for more detailed derivations and^{30,31} for additional applications). The innovation starts with the method typically used for computing the spatial gradient of a quantity measured by four spacecraft (e.g., see ref. 51) and applies that technique to each of the FPI’s Dual Electron Spectrometer (DES) velocity-space measurement bins. To visualize the component of the electron gradient distribution parallel to the magnetic field, the vector quantity ∇f_e is projected onto the magnetic field direction: $\nabla_{\parallel} f_e = \nabla f_e \cdot \hat{\mathbf{b}}$.

The quantity ∇f_e may be thought of as an ordinary vector that has three components, i.e., $\partial f_e/\partial x$, $\partial f_e/\partial y$, and $\partial f_e/\partial z$, each of which has a velocity-space structure in \mathbf{v} that can be visualized in the same way one typically visualizes the distribution $f_e(\mathbf{v})$. Alternatively, one may also combine spatial and velocity-space coordinates and represent ∇f_e as a group of vectors attached to each FPI measurement bin throughout velocity space. In this representation, one imagines superimposing spatial (x, y, z) and velocity space (v_x, v_y, v_z) coordinates, so that the vector ∇f_e at each point in the velocity space points in the spatial direction of increasing phase space density. Taking the sum of all of these vectors corresponds to integrating ∇f_e over velocity space d^3v , and thus results in a single vector corresponding to the electron fluid’s density gradient: $\int \nabla f_e d^3v = \nabla \int f_e d^3v = \nabla n_e$.

Data availability

The MMS data are publicly available at <https://lasp.colorado.edu/mms/sdc/public/>. The PIC data are available from the corresponding author upon request.

Code availability

The simulations are performed using the Vector Particle-in-Cell (VPIC) code, which is available at: <https://github.com/lanl/vpic>. The MMS and PIC data are analyzed using IDL code available from the corresponding author upon request.

Received: 7 August 2025; Accepted: 30 December 2025;

Published online: 10 January 2026

References

- Burch, J. L., Moore, T. E., Torbert, R. B. & Giles, B. L. Magnetospheric multiscale overview and science objectives. *Space Sci. Rev.* **199**, 5–21 (2016).
- Burch, J. L. et al. Electron-scale measurements of magnetic reconnection in space. *Science* **352**, aaf2939 (2016).
- Hesse, M., Aunai, N., Sibeck, D. & Birn, J. On the electron diffusion region in planar, asymmetric, systems. *Geophys. Res. Lett.* **41**, 8673–8680 (2014).
- Chen, L.-J., Hesse, M., Wang, S., Bessho, N. & Daughton, W. Electron energization and structure of the diffusion region during asymmetric reconnection. *Geophys. Res. Lett.* **43**, 2405–2412 (2016).
- Bessho, N., Chen, L.-J. & Hesse, M. Electron distribution functions in the diffusion region of asymmetric magnetic reconnection. *Geophys. Res. Lett.* **43**, 1828–1836 (2016).
- Genestreti, K. J. et al. MMS observation of asymmetric reconnection supported by 3-D electron pressure divergence. *J. Geophys. Res. Space Phys.* **123**, 1806–1821 (2018).
- Shuster, J. R. et al. MMS measurements of the Vlasov equation: Probing the electron pressure divergence within thin current sheets. *Geophys. Res. Lett.* **46**, 7862–7872 (2019).
- Ng, J., Egedal, J., Le, A., Daughton, W. & Chen, L.-J. Kinetic structure of the electron diffusion region in antiparallel magnetic reconnection. *Phys. Rev. Lett.* **106**, 065002 (2011).
- Bessho, N., Chen, L.-J., Shuster, J. R. & Wang, S. Electron distribution functions in the electron diffusion region of magnetic reconnection: Physics behind the fine structures. *Geophys. Res. Lett.* **41**, 8688–8695 (2014).
- Shuster, J. R. et al. Spatiotemporal evolution of electron characteristics in the electron diffusion region of magnetic reconnection: Implications for acceleration and heating. *Geophys. Res. Lett.* **42**, 2586–2593 (2015).
- Torbert, R. B. et al. Electron-scale dynamics of the diffusion region during symmetric magnetic reconnection in space. *Science* **362**, 1391–1395 (2018).
- Nakamura, R. et al. Structure of the current sheet in the 11 July 2017 electron diffusion region event. *J. Geophys. Res.: Space Phys.* **124**, 1173–1186 (2019).
- Shuster, J. R. et al. Hodographic approach for determining spacecraft trajectories through magnetic reconnection diffusion regions. *Geophys. Res. Lett.* **44**, 1625–1633 (2017).
- Afshari, A. S., Howes, G. G., Kletzing, C. A., Hartley, D. P. & Boardsen, S. A. The importance of electron Landau damping for the dissipation of turbulent energy in terrestrial magnetosheath plasma. *J. Geophys. Res. Space Phys.* **126**, e2021JA029578 (2021).
- McCubbin, A. J., Howes, G. G. & TenBarge, J. M. Characterizing velocity-space signatures of electron energization in large-guide-field collisionless magnetic reconnection. *Phys. Plasmas* **29**, 052105 (2022).
- Chen, C., Klein, K. & Howes, G. Evidence for electron Landau damping in space plasma turbulence. *Nat. Commun.* **10**, 740 (2019).
- Howes, G. G. A prospectus on kinetic heliophysics. *Phys. Plasmas* **24**, 055907 (2017).
- Cassak, P. A., Barbhuiya, M. H., Liang, H. & Argall, M. R. Quantifying energy conversion in higher-order phase space density moments in plasmas. *Phys. Rev. Lett.* **130**, 085201 (2023).
- Barbhuiya, M. H. et al. Higher-order nonequilibrium term: Effective power density quantifying evolution towards or away from local thermodynamic equilibrium. *Phys. Rev. E* **109**, 015205 (2024).
- Klein, K. G. & Howes, G. G. Measuring collisionless damping in heliospheric plasmas using field-particle correlations. *Astrophys. J. Lett.* **826**, L30 (2016).
- Phan, T. D. et al. Electron magnetic reconnection without ion coupling in Earth’s turbulent magnetosheath. *Nature* **557**, 202–206 (2018).
- Payne, D. S. et al. In-situ observations of the magnetothermodynamic evolution of electron-only reconnection. *Commun. Phys.* **8**, 36 (2025).

23. Liu, Y.-H. et al. First-principles theory of the rate of magnetic reconnection in magnetospheric and solar plasmas. *Commun. Phys.* **5**, 97 (2022).
24. Liu, Y.-H. et al. An analytical model of “electron-only” magnetic reconnection rates. *Commun. Phys.* **8**, 128 (2025).
25. Sharma Pyakurel, P. et al. Transition from ion-coupled to electron-only reconnection: Basic physics and implications for plasma turbulence. *Phys. Plasmas* **26**, 082307 (2019).
26. Egedal, J. et al. Spacecraft observations and analytic theory of crescent-shaped electron distributions in asymmetric magnetic reconnection. *Phys. Rev. Lett.* **117**, 185101 (2016).
27. Rager, A. C. et al. Electron crescent distributions as a manifestation of diamagnetic drift in an electron-scale current sheet: Magnetospheric multiscale observations using new 7.5 ms fast plasma investigation moments. *Geophys. Res. Lett.* **45**, 578–584 (2018).
28. Pollock, C. et al. Fast plasma investigation for magnetospheric multiscale. *Space Sci. Rev.* **199**, 331–406 (2016).
29. Hasegawa, H. et al. Advanced methods for analyzing in-situ observations of magnetic reconnection. *Space Sci. Rev.* **220**, 68 (2024).
30. Shuster, J. R. et al. Structures in the terms of the Vlasov equation observed at earth’s magnetopause. *Nat. Phys.* **17**, 1056–1065 (2021).
31. Shuster, J. R. et al. Temporal, spatial, and velocity-space variations of electron phase space density measurements at the magnetopause. *J. Geophys. Res.: Space Phys.* **128**, e2022JA030949 (2023).
32. Vlasov, A. A. The vibrational properties of an electron gas. *J. Exp. Theor. Phys.* **8**, 29–33 (1938).
33. Vlasov, A. A. On the kinetic theory of an assembly of particles with collective interaction. *J. Phys. (USSR)* **9**, 25–40 (1945).
34. Ergun, R. E. et al. Magnetospheric multiscale satellites observations of parallel electric fields associated with magnetic reconnection. *Phys. Rev. Lett.* **116**, 235102 (2016).
35. Gurnett, D. A. & Bhattacharjee, A. *Introduction to Plasma Physics: With Space and Laboratory Applications* (New York: Cambridge University Press, 2005).
36. Denton, R. E. et al. Motion of the mms spacecraft relative to the magnetic reconnection structure observed on 16 October 2015 at 1307 ut. *Geophys. Res. Lett.* **43**, 5589–5596 (2016).
37. Gershman, D. J. et al. Spacecraft and instrument photoelectrons measured by the dual electron spectrometers on mms. *J. Geophys. Res.: Space Phys.* **122**, 11,548–11,558 (2017).
38. Argall, M. R. et al. Theory, observations, and simulations of kinetic entropy in a magnetotail electron diffusion region. *Phys. Plasmas* **29**, 022902 (2022).
39. Liu, Y.-H., Daughton, W., Karimabadi, H., Li, H. & Roytershteyn, V. Bifurcated structure of the electron diffusion region in three-dimensional magnetic reconnection. *Phys. Rev. Lett.* **110**, 265004 (2013).
40. Christopher, B., Dorelli, J., da Silva, D., Khazanov, G. & Dibyendu, S. MARBLE: How to make an open science global magnetosphere code? (2023).
41. Bard, C. & Dorelli, J. High-performance computational magnetohydrodynamics with python. *arXiv* (2025).
42. Webster, J. M. et al. Magnetospheric multiscale dayside reconnection electron diffusion region events. *J. Geophys. Res. Space Phys.* **123**, 4858–4878 (2018).
43. Wilder, F. D. et al. The role of the parallel electric field in electron-scale dissipation at reconnecting currents in the magnetosheath. *J. Geophys. Res. Space Phys.* **123**, 6533–6547 (2018).
44. Spinnangr, S. F. et al. Electron behavior around the onset of magnetic reconnection. *Geophys. Res. Lett.* **49**, e2022GL102209 (2022).
45. Norgren, C. et al. Phase-space contributions to pressure and stress tensors in the electron diffusion region of magnetic reconnection. *Phys. Plasmas* **32**, 052109 (2025).
46. Ng, J., Egedal, J., Le, A. & Daughton, W. Phase space structure of the electron diffusion region in reconnection with weak guide fields. *Phys. Plasmas* **19**, 112108 (2012).
47. Miles, D. M. et al. The tandem reconnection and cusp electrodynamics reconnaissance satellites (tracers) mission. *Space Sci. Rev.* **221**, 61 (2025).
48. Ergun, R. E. et al. The axial double probe and fields signal processing for the mms mission. *Space Sci. Rev.* **199**, 167–188 (2016).
49. Russell, C. T. et al. The magnetospheric multiscale magnetometers. *Space Sci. Rev.* **199**, 189–256 (2016).
50. Torbert, R. B. et al. The fields instrument suite on mms: Scientific objectives, measurements, and data products. *Space Sci. Rev.* **199**, 105–135 (2016).
51. Harvey, C. C. *Spatial Gradients and the Volumetric Tensor*, 307–322 (ISSI Scientific Reports Series, in *Analysis Methods for Multi-Spacecraft Data*, edited by G. Paschmann and P. W. Daly, 1998).
52. Poje, L. & Masters, J. NASA spacecraft finds new magnetic process in turbulent space. *NASA Goddard Space Flight Center, Scientific Visualization Studio* (2018).

Acknowledgements

We especially thank the MMS instrument teams for their dedication and commitment to providing unprecedented, high-quality datasets. J.R.S. was supported by NASA Grants 80NSSC23K1152 and 80NSSC23K1600, and grants to the MMS FIELDS team. Additionally, J.R.S. thanks E. Raymond and K. Springfield for their encouragement and reminder that electrons can smile (even though they’re negative!). P.A.C. was supported by NASA grant 80NSSC23K0409 and NSF grant PHY-2308669.

Author contributions

J.R.S. performed the MMS multi-spacecraft data analysis, analyzed the PIC simulation data, and prepared the manuscript. N.B. assisted with the interpretation of the electron distribution data from the PIC simulation. J.C.D. offered insights into both the MMS and PIC data, and provided institutional support for the project team. D.J.G. helped with the interpretation of the multi-spacecraft FPI electron DES data. J.M.H.B. aided in the analysis and interpretation of the MMS multi-spacecraft data. H.G. helped with the analysis and interpretation of the MMS electron gradient distributions. J.N. assisted with the interpretation of the PIC simulation results. L.J.C. provided valuable insights during the data analysis and manuscript preparation. R.B.T. offered insights regarding the interpretation of the MMS electric and magnetic fields data. J.L.B. gave valuable feedback to support the manuscript preparation. B.L.G. supported the project and helped to ensure quality of the MMS and FPI data. R.E.D. offered detailed feedback regarding the interpretation of the MMS data during the manuscript preparation. P.A.C. helped with the theory and simulation interpretation. M.H.B. assisted with clarifying the implications and interpretation of the results. S.J.S. offered valuable expertise regarding the organization and presentation of the results. Y.H.L. provided technical expertise concerning the PIC simulation results and manuscript preparation. C.N. contributed to the interpretation of the MMS and PIC electron distribution function results. D.E.d.S. supported the project with the preparation of helpful data analysis tools. K.J.G. contributed to the manuscript organization and preparation. S.V.H. assisted with the interpretation of the MMS fields and particle datasets. M.R.A. provided useful feedback during the data analysis and manuscript preparation. H.K. offered important perspective into the interpretation and implication of the electron gradient distribution results. A.T.M. assisted with the MMS data interpretation. R.N. offered important perspectives regarding the MMS data and manuscript preparation. H.L. helped with the interpretation of the PIC simulation predictions. V.M.U. gave helpful insights during the manuscript preparation and organization phases. A.A. assisted with the interpretation of the detailed MMS electron velocity-space data. D.S.P. offered important feedback and contributions during the manuscript preparation.

Competing interests

The authors declare no competing interests.

Additional information

Supplementary information The online version contains supplementary material available at <https://doi.org/10.1038/s42005-026-02489-8>.

Correspondence and requests for materials should be addressed to Jason R. Shuster.

Peer review information *Communications Physics* thanks Jim Schroeder, Jun Zhong, Lev M. Zelenyi and the other, anonymous, reviewer(s) for their contribution to the peer review of this work. A peer review file is available.

Reprints and permissions information is available at <http://www.nature.com/reprints>

Publisher's note Springer Nature remains neutral with regard to jurisdictional claims in published maps and institutional affiliations.

Open Access This article is licensed under a Creative Commons Attribution-NonCommercial-NoDerivatives 4.0 International License, which permits any non-commercial use, sharing, distribution and reproduction in any medium or format, as long as you give appropriate credit to the original author(s) and the source, provide a link to the Creative Commons licence, and indicate if you modified the licensed material. You do not have permission under this licence to share adapted material derived from this article or parts of it. The images or other third party material in this article are included in the article's Creative Commons licence, unless indicated otherwise in a credit line to the material. If material is not included in the article's Creative Commons licence and your intended use is not permitted by statutory regulation or exceeds the permitted use, you will need to obtain permission directly from the copyright holder. To view a copy of this licence, visit <http://creativecommons.org/licenses/by-nc-nd/4.0/>.

© The Author(s) 2026